Multifunctional Lightweight Radiators for Small-Satellite Thermal Control

Karl Pederson,* Sam Keller,† Daniel Kindem,‡ Hayden Hommes,§ and Ognjen Ilic¶
University of Minnesota, Minneapolis, Minnesota 55455

https://doi.org/10.2514/1.A36693

Thermal management in small satellites, such as CubeSats, is constrained by limited radiative area and strict mass budgets, necessitating the development of radiator structures that are simultaneously lightweight, thermally conductive, and mechanically robust. This work presents a topology-optimization and design-space analysis framework for multifunctional lightweight radiators that achieve high specific stiffness and high effective thermal conductivity through structural and thermal optimization. Density-based optimization produces hierarchical architectures that naturally form continuous cavities suitable for high-conductivity channels such as embedded heat pipes. This study reveals scaling behavior and optimal tradeoffs between mass, stiffness, effective thermal conductivity, and the dynamic response of the optimized microarchitectures that form the core of the small-satellite radiator. Coupled structural–thermal analysis shows that prescribed cavities used as thermal channels yield nearly isothermal radiating surfaces, which confirms efficient lateral and transverse heat flow through the radiator. This integrated design approach contributes toward the development of thermomechanically optimized radiator panels for small-scale spacecraft, with the aim of enabling compact, efficient, and lightweight thermal control systems.

Nomenclature

A	=	area
E	=	Young's modulus
F	=	applied load
J	=	total strain energy
K	=	stiffness
k	=	thermal conductivity
L	=	radiator length
N	=	number of iterations
N_{hp}	=	number of heat pipes
p	=	penalization coefficient
Q_r	=	radiated heat transfer
R	=	filter radius
T	=	temperature
t	=	radiator thickness
V	=	volume
w	=	radiator width
β	=	filtering parameter
γ	=	volume fraction
δ	=	deflection
ε	=	strain, emissivity
η_f	=	fin efficiency
θ	=	material density variable
θ_0	=	minimum density
θ_β	=	projection threshold
ρ	=	mass density
σ	=	stress

Subscripts

base	=	radiator base
eff	=	effective property
Ω	=	region of interest

Received 31 December 2025; accepted for publication 1 July 2026; published online 24 July 2026.

*Graduate Research Assistant, Department of Mechanical Engineering.
†NASA Space Technology Graduate Research Opportunities Fellow, Department of Mechanical Engineering.
‡Graduate Research Assistant, Department of Mechanical Engineering.
§Undergraduate Research Assistant, Department of Mechanical Engineering.
¶Assistant Professor, Department of Mechanical Engineering; ilic@umn.edu (Corresponding Author).

I. Introduction

LIGHTWEIGHT structures that combine high thermal conductivity and mechanical stiffness are increasingly important for spacecraft and satellite applications. In orbit, spacecraft can undergo repeated and drastic transitions between intense solar irradiation and eclipse, producing large thermal fluctuations that must be managed with systems with limited radiative surface area [1]. For small satellites and microsystems such as CubeSats [2], these constraints are even more severe: small system size limits the available area for heat rejection, while ever-increasing onboard power requirements necessitate greater heat transport from the inside of the spacecraft bus to outer space [3–6]. Deployable radiator panels—thin, large-area structures that are usually body-mounted or extendable—are widely used to increase radiating area and therefore rejected heat [7–10]. However, these radiators must simultaneously satisfy demanding mechanical and thermal criteria: they must maintain structural rigidity while minimizing mass, provide high thermal conductivity, and limit the coupling into on-orbit mechanical disturbances. Efforts to reduce the density of solid-panel radiators while maintaining stiffness have produced sandwich composites with lightweight honeycomb cores [11], where additional components, such as heat pipes or vapor chambers, are typically added to improve lateral heat-spreading capabilities and achieve sufficiently high thermal conductivity [12–19]. In a typical implementation, the structural core and heat-transport elements are designed sequentially, where a low-density core may first be selected for mechanical performance, while heat pipes or other conductive elements are then integrated to improve thermal spreading. However, this sequential approach can introduce tradeoffs in the combined structure. Integrating heat pipes into an otherwise optimized core may interrupt load-bearing pathways and reduce stiffness, while a core primarily selected for mechanical performance may provide suboptimal lateral heat spreading. Approaches to mechanical and thermal codesign have explored parameter sweeps within predefined, parameterized design spaces, such as truss or lattice cores [20], without accessing the broader topology-optimization design space to address the tight size and weight constraints that are inherent to small-satellite and CubeSat platforms. For CubeSats carrying precision payloads such as optical imagers or laser communication terminals, deployed appendages such as radiators can couple mechanical disturbances into line-of-sight jitter, degrading payload performance [21–23]. For example, broadband disturbances from

CubeSat wheel assemblies have been characterized up to 500 Hz [24], which overlaps with the natural frequencies of CubeSat-sized radiators and motivates the development of radiator designs with high specific stiffness and high natural frequencies for improved pointing stability.

In this work, we introduce a combined topology-optimization and design-space analysis framework for multifunctional radiator architectures tailored to small satellites and CubeSat platforms (Fig. 1). In a systematic analysis, this approach reveals lightweight structures with high specific stiffness and naturally forming continuous cavities that could host embedded heat pipes, thereby enabling high effective thermal conductivity at low density. We implement this approach using density-based topology optimization [25–27] to design microarchitected radiator profiles that maximize specific stiffness (stiffness normalized by density) while forming hierarchical "tree-like" motifs that concentrate material along principal load paths and enhance both mechanical stiffness and thermal conduction pathways.

Our manuscript is organized as follows. First, we systematically explore the relationship between radiator thickness, volume fraction, and material type, revealing mass/stiffness/thermal conductivity Pareto fronts that guide lightweight design for CubeSat-compatible radiators. Next, we evaluate the optimized architectures for bending stiffness, vibration response, and heat-transfer performance. Third, through coupled structural–thermal analysis, we show that voids formed during optimization can act as natural conduits for embedded heat pipes with the potential to achieve nearly isothermal radiator surfaces with high (>90%) radiator efficiency. Finally, we compare free-geometry and constrained-geometry optimizations (where fixed circular cavities represent standardized heat-pipe profiles) to demonstrate that superior thermal uniformity can be achieved without compromising the dynamic response.

II. Radiator Topology Optimization

We begin by using two-dimensional topology optimization to design radiator geometries that achieve high specific modulus, defined as Young's modulus normalized by the effective density of the structure. The topology optimization used here is motivated by the extruded geometry of radiator panels and by the fact that the panel length is a dominant direction for both thermal transport and mechanical response. Thermally, heat must be transported away from the spacecraft and distributed along the radiator length before being rejected from the radiating surface. Mechanically, the lowest-frequency mode of a slender deployed radiator panel is typically associated with bending along the same length axis. For the idealized radiator architectures considered here, in which the material properties, cross section, and heat-pipe/channel regions are assumed to be repeated along the extruded direction, optimizing the cross section thus captures the primary tradeoff between thermally conductive pathways and load-bearing pathways. Figure 2 illustrates

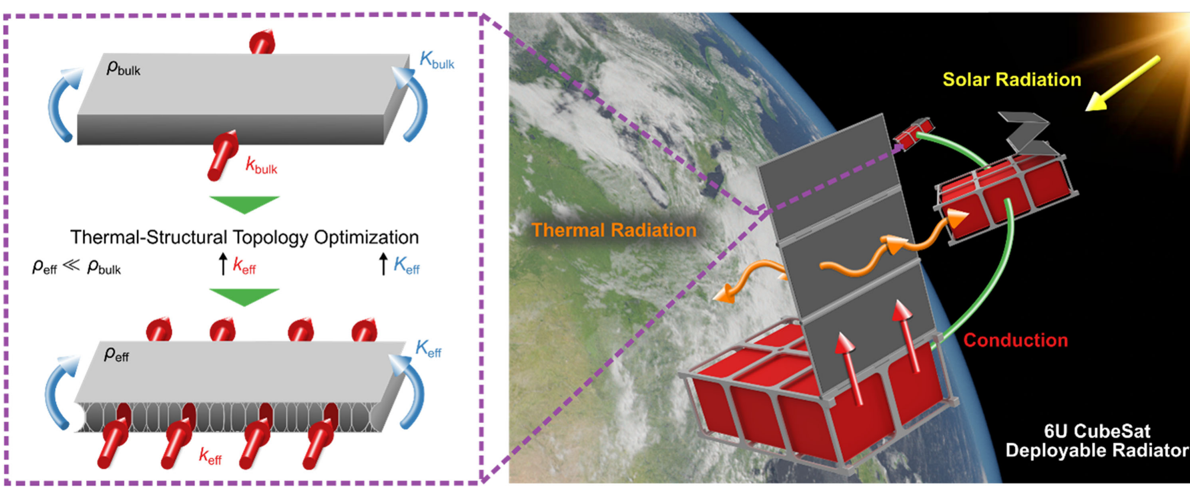

Fig. 1 Conceptual illustration of thermal–structural design enabling topology-optimized radiators with high stiffness and thermal conductivity for small spacecraft, such as the illustrated 6U CubeSat.

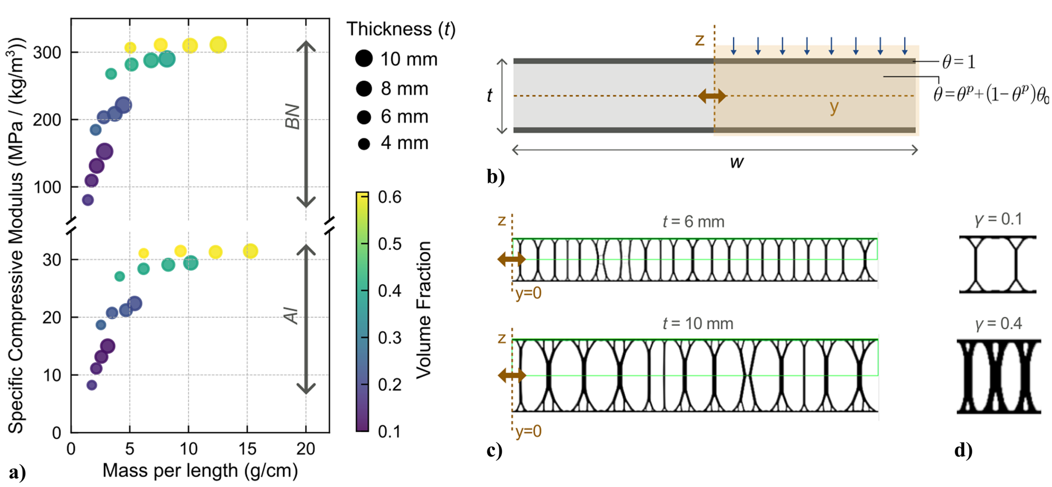

Fig. 2 a) Pareto front of specific compressive modulus versus mass per length. b) Topology-optimization domain. c) Representative optimized half-geometries (mirror plane at $y = 0$). d) Enlarged topology patterns showing porosity-dependent morphology.

the approach taken to design cross-sectional geometries. In this formulation, a cross section (y-z plane) is optimized to minimize the functional:

$$J(\theta) = \int_{\Omega} \boldsymbol{\sigma}(\theta) : \boldsymbol{\varepsilon}(\theta)\, \mathrm{d}\Omega \tag{1}$$

where $\boldsymbol{\sigma}$ and $\boldsymbol{\varepsilon}$ are the stress and strain tensors, respectively, Ω denotes the system domain, and θ represents the normalized density, which is the design variable. The functional $J(\theta)$ denotes the compliance, whose minimization corresponds to the maximization of stiffness. This optimization is subject to the volume constraint that restricts the fraction of the domain that will be occupied by solid material:

$$0 \leq \int_{\Omega} \theta\, \mathrm{d}\Omega \leq \gamma V \tag{2}$$

where θ denotes the density profile normalized to [0, 1], V is the domain volume, and γ is the volume fraction. We employ the solid isotropic material with penalization (SIMP) method of topology optimization implemented in COMSOL Multiphysics [28]. For a given unit cell, symmetry is enforced across both the horizontal and vertical axes. We focus on radiator dimensions compatible with the CubeSat unit length (10 cm). For a fixed radiator width $w = 10$ cm, the radiator thickness $t = 4$, 6, 8, and 10 mm; the volume fraction constraint $\gamma = 0.1$, 0.2, 0.4, and 0.6; and the material is varied (a high-modulus ceramic (boron nitride [29]) and a moderate-modulus but thermally conductive metal alloy (Al–Li 8090 alloy [30])). These parameter ranges are chosen to represent the practical design space for lightweight, thin radiators suitable for small-satellite thermal management. Default optimization parameters were set as $\theta_0 = 10^{-3}$, $\theta_\beta = 0.5$, and R as the minimum mesh element size. Additionally, $p = 3$ and $\beta = 5$ were chosen for an initial optimization over a fixed number of iterations ($N = 100$). The top and bottom faces of the unit cell are fixed to be solid (density $\theta = 1$), while the central region has density from SIMP [25,31]:

$$\theta = \theta^p + (1 - \theta^p)\theta_0 \tag{3}$$

where θ_0 is the minimum allowable density. In the design region, the corresponding Young's modulus is scaled, per SIMP, to be $E = E_{\text{solid}}\theta_p$, where E_{solid} is the Young's modulus of the solid material. Following the initial optimizations, a continuation study was conducted to enhance binarization of the material distribution. Starting from each previously optimized structure, the penalization parameters p and β were progressively increased through the sequence (5, 5), (5, 10), and (10, 20). At each step, the solution from the prior stage was used as the initial starting point. After completing the continuation study, a binarized topology was extracted using a threshold-based discretization filter (the filter is applied to the filtered θ variable). The filter threshold/cutoff was adjusted to the value that closely preserves the original volume fraction specified at the beginning of each optimization while maintaining the connected topology of the structure.

As a result of topology optimization, tree-like motifs emerge. These motifs reflect the optimizer's tendency to concentrate material along principal load paths, forming hierarchical, branching structures. When thickness increases, fewer "tree" motifs are produced, leading to fewer but larger cavities (Fig. 2c). Higher volume fractions (0.4 and 0.6) lead to smaller cavities and less branching of small features (Fig. 2d). However, as both thickness and volume fraction vary, these tree motifs are consistently present in the final structures. Because the resulting cavities are continuous, convex, and regularly spaced, they can serve as natural channels for embedding heat pipes or other high-conductivity pathways. Therefore, this optimization approach leads to structures with high specific stiffness and the capability to incorporate heat pipes to achieve high thermal conductivity.

III. Thermomechanical Analysis of Radiator Performance

We next evaluate the performance of the optimized geometries by examining the relationship between specific compressive modulus and mass, revealing key tradeoffs across design parameters. Specific modulus is obtained from the equivalent homogenized modulus of the optimized cross section divided by the effective density (determined from the spatially averaged material density profile):

$$E_{\text{spec}} = \left(\frac{E_{\text{eff}}}{\rho_{\text{eff}}}\right) = \frac{E_{\text{eff}} A_{\Omega}}{\int_{\Omega} \rho\, \mathrm{d}A} \tag{4}$$

Here, ρ_{eff} denotes the effective density and E_{eff} the effective modulus defined as $E_{\text{eff}} = \sigma_c/\varepsilon_c$, where σ_c and ε_c are the computationally extracted stress and strain from finite element analysis. This relationship is shown in Fig. 2a and highlights how design variables influence specific modulus and mass per unit length. At low volume fractions (0.1–0.2), increasing radiator thickness leads to significantly higher specific modulus with little mass penalty. In contrast, at higher volume fractions (0.4–0.6), radiator thickness has little impact on stiffness while incurring significant added mass. A similar trend appears when changing the volume fraction at different thicknesses: increasing infill at lower thicknesses (4–6 mm) has a significant positive impact with a small increase in mass; however, the mass penalty becomes exacerbated when increasing the volume fraction at higher thicknesses (8–10 mm). These results indicate that the ability to increase the effective modulus decreases rapidly once the structure becomes relatively dense, as additional material no longer contributes meaningfully to load-bearing capacity. We note that changing the structural properties of the material has little impact on the optimized topologies or overall trends, suggesting that geometric design, rather than the intrinsic material modulus, dominates the stiffness trends in this regime. The results suggest that the volume fraction is the dominant factor in determining the specific stiffness of the material. From a design standpoint, these findings imply that low-to-intermediate radiator thicknesses (4–6 mm) combined with moderate volume fractions (0.2–0.4) achieve an optimal balance between stiffness and mass, offering a practical guideline for lightweight radiator design.

To investigate how the optimized geometries perform under bending, we extend our analysis to three-dimensional extrusions of the radiator cross sections. Figure 3a visualizes the parameters of interest, which now include varying length (L), alongside thickness (t), and volume fraction (γ). This three-dimensional extrusion allows us to capture deformation and stiffness characteristics that cannot be fully represented in a two-dimensional compression analysis. To analyze the extruded structures in bending, the front face of the radiator was fixed, with a tip load applied uniformly to the back face. Thus, the effective bending modulus becomes:

$$E_{\text{eff}} = \frac{4FL^3}{\delta w t^3} \tag{5}$$

where L is the radiator length, w is the radiator width, t is the radiator thickness, and F and δ are the force and displacement numerically obtained from finite element analysis. The specific bending stiffness is then calculated as:

$$E_{\text{spec}} = \left(\frac{E_{\text{eff}}}{\rho_{\text{eff}}}\right) = \frac{E_{\text{eff}} V_{\Omega}}{\int_{\Omega} \rho\, \mathrm{d}V} \tag{6}$$

Figure 3b shows the relationship between specific bending modulus and mass for topology-optimized cross sections extruded to various lengths. Here, decreasing volume fraction results in both higher specific modulus and lower mass. This behavior indicates that high-specific-bending-modulus designs naturally emerge at low infill levels, where material is distributed primarily along load paths. This same trend is present with radiator thickness, effectively removing the tradeoff between stiffness and mass that was present

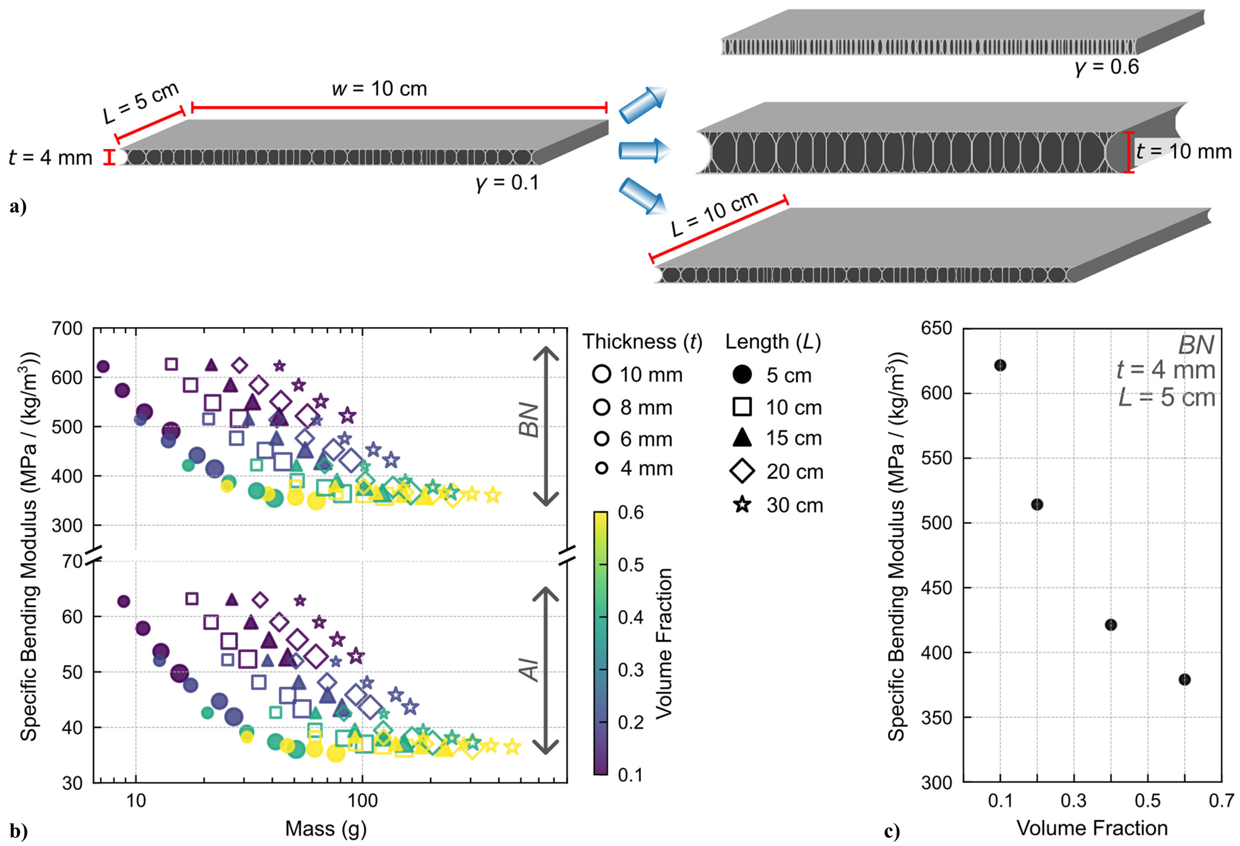

Fig. 3 a) Parameter design space for an extruded radiator. b) Specific bending modulus versus mass. c) Specific bending modulus versus volume fraction.

under compression. When two-dimensional topologies optimized for compressive stiffness are subjected to bending boundary conditions, the solid, thick material becomes the lower-performance limit (in contrast to the upper limit for uniform compression). This inversion reflects the geometric inefficiency of solid sections in bending, where stiffness more strongly depends on the distribution of material about the neutral axis. The removal of the tradeoff between mass and specific stiffness renders fabrication constraints and absolute bending stiffness requirements the limiting factors. Among these, volume fraction (a common constraint in additive manufacturing) plays a particularly important role in determining achievable stiffness. Figure 3c shows a characteristic relationship between specific bending modulus and volume fraction (here shown for a 4-mm-thick (t), 5-cm-long (L) radiator made of BN). Increasing the volume fraction from 0.1 to 0.6 results in approximately a 40% decrease in specific modulus. This trend highlights the penalty of excessive infill, where added material increases mass without proportionally improving bending modulus. Low-thickness (4 mm), low-volume-fraction (0.1) radiator cross sections provide high specific bending modulus and low mass, enabling longer radiators for high-power heat rejection.

Next, we analyze the dynamic response of optimized radiator structures to assess the potential for coupling to mechanical disturbances and on-orbit vibrations. Figure 4a depicts the profiles of the three lowest vibrational modes of a microarchitected radiator with a clamped edge. While stiffness is an important design metric for lightweight deployed structures, natural frequency (eigenfrequency) considerations are also important because low resonant frequencies can increase dynamic deflection under reaction-wheel or attitude-control disturbances. Figure 4b shows the Pareto front between the fundamental (lowest-mode) eigenfrequency and mass for various radiator thicknesses, volume fractions, and radiator lengths. Of these three parameters, we observe that the infill of a cross section has the least impact on the fundamental-mode frequency. Raising the volume fraction causes a small decrease in eigenfrequency and, thus, is undesirable when designing for vibrations. Radiator thickness has a positive correlation with eigenfrequency, but the benefit is less pronounced with an increase in mass, highlighting the challenge of maintaining both low mass and high natural frequency. The most influential factor affecting the fundamental frequency of an extended radiator is its length. Figure 4c highlights this impact for the example of a 4-mm-thick, 10%-infill radiator. Here, the fundamental frequency of a long (30 cm) radiator is almost 100× lower than that of a short (5 cm) radiator. We note that the fundamental frequency of a long radiator can be increased by increasing its thickness. However, this increase in eigenfrequency leads to an additional penalty in mass. Therefore, optimizing for reduced dynamic compliance requires a balance between structural geometry and fill fraction, with length emerging as the dominant design constraint.

We examine the heat transfer potential of the optimized radiator structures with a heat transfer analysis in which voids between tree-like motifs are treated as embedded heat pipes, as illustrated in Fig. 5. The selected voids are spaced to maintain an approximately w/N_{hp} spaced separation along the width of the radiator from its center. The analysis models the upper-right quadrant of the structure, with symmetry assumed across both the horizontal and vertical axes. Surfaces in contact with heat pipe cavities are treated as isothermal, with a radiative boundary at the top face and adiabatic conditions elsewhere. This assumption of isothermal heat pipe boundaries is a suitable first-order approximation, given the high effective axial thermal conductance of conventional spacecraft heat pipes relative to the surrounding microarchitected radiator material [32]. The isothermal assumption is useful because it isolates the role of the optimized core topology in distributing heat to the radiating surface, without requiring a detailed thermofluidic model of a specific heat-pipe implementation. In practice, two-phase-flow pressure drops and irregular channel shapes could reduce the effective heat-transport capacity of the embedded channel, producing temperature variation along the channel. To evaluate this effect, the Supplementary Materials include a sensitivity study in

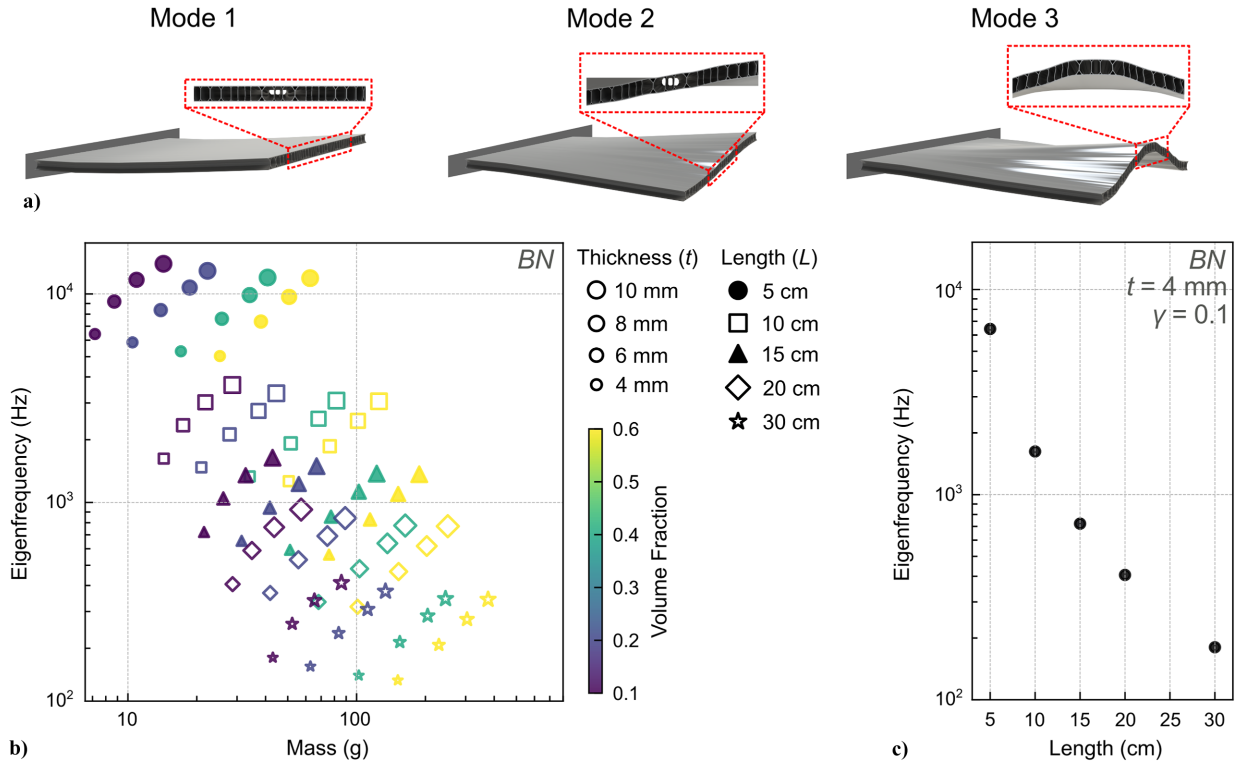

Fig. 4 Dynamic response of optimized radiators. a) Representative mode shapes for the first three modes. b) Fundamental eigenfrequency versus mass. c) Fundamental eigenfrequency versus radiator length.

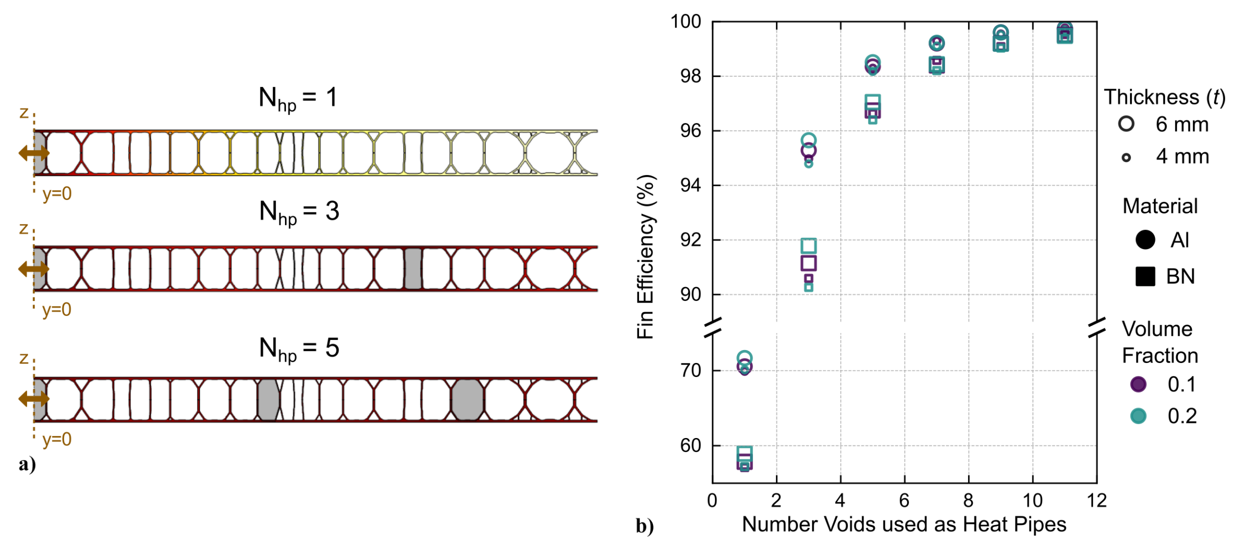

Fig. 5 Thermal analysis of optimized radiators with embedded heat channels. a) Temperature profiles with an increasing number of heat channels. b) Thermal fin efficiency versus number of heat channels.

which the isothermal boundary condition is replaced by finite-conductivity channel domains with varying effective conductivity. This analysis quantifies when the predicted radiated-power performance approaches the isothermal-channel limit. Generally, an efficiency metric η_f can be defined for a radiator as follows:

$$\eta_f = \frac{Q_{\mathrm{r,actual}}}{Q_{\mathrm{r,ideal}}} = \frac{\int_A \varepsilon T(x,y)^4 \, \mathrm{d}A}{A\varepsilon T_{\mathrm{base}}^4} \tag{7}$$

where $Q_{\mathrm{r,ideal}} = A\varepsilon\sigma T_{\mathrm{base}}^4$ is the rejected heat if the radiator surfaces are isothermal at the base temperature T_{base}, A is the radiator area, ε is the surface emissivity, and $Q_{\mathrm{rad,actual}} = \int_A \varepsilon T(x,y)^4 \, \mathrm{d}A$ is the actual rejected heat from the radiator. All radiative heat-transfer calculations assume a constant hemispherical-total emissivity of unity, and radiative heat loss is modeled using the Stefan–Boltzmann law under deep-space thermal sink conditions. The normalized comparisons presented in this analysis are insensitive to the specific emissivity value, as all designs are evaluated under identical surface and environmental conditions.

As the number of heat pipes N_{hp} in the radiator increases, the temperature distribution along the radiator face becomes more uniform (Fig. 5a). This behavior reflects improved lateral heat spreading as additional heat pipes provide efficient conduction pathways through the structure. Figure 5b compares the radiated power from the top surface to that of an isothermal surface as a function of the number of voids (N_{hp}) selected as heat pipes. When the number of embedded heat pipes is low (1–2), conduction through the microarchitected lattice strongly influences the amount of radiated power, and the limited conduction pathways lead to localized temperature gradients. These temperature gradients are undesirable due to the thermal stress that may occur. The Supplementary Materials contain a mesh sensitivity study that confirms the convergence of the temperature solution when localized temperature gradients are present. As the number of heat pipes increases, conduction through them begins to dominate the system. Beyond approximately three embedded heat pipes, the radiator approaches a nearly isothermal condition, marking a transition from lattice-dominated to heat-pipe-dominated thermal transport. This shift results in a 25–30% increase in emitted power as the number of heat pipes increases from one to three. At higher heat pipe counts (7+), the surface becomes effectively isothermal, radiating more than 99% of the power of an isothermal blackbody surface at $N_{\mathrm{hp}} = 11$. Together, these results demonstrate that selectively utilizing cavities formed during topology optimization enables multifunctional structures that combine high mechanical stiffness with nearly uniform thermal performance and high fin efficiency.

IV. Constrained Topology Design of Radiators with Cylindrically Shaped Heat Pipes

To compare the previous free-geometry optimization with a more constrained design strategy, we perform a topology optimization that incorporates fixed, circular heat pipe cavities at prescribed locations. We adopt this constrained optimization approach because, although the convex cavities in Fig. 5 could in principle function as heat channels, their varying and irregular shapes and sizes could complicate fabrication standardization. As an alternative approach, Fig. 6a shows a topology optimization that constrains the geometry by fixing circular cavities at specific positions spaced w/N_{hp} from the radiator center to serve as thermal channels/heat pipes. Here, rather than selecting arbitrary cavities between tree motifs as thermal channels, conventional circular cavities with 0.2 mm thickness are defined in advance. This modification enables direct control over the spacing and orientation of the thermal channels while maintaining a structurally optimized surrounding architecture. Outside the protected circular cavity regions, where the density variable is fixed, the microarchitecture is optimized in two dimensions for specific stiffness. Figure 6b shows the results of the constrained optimization. We observe that as the number of heat pipe cavities increases, the specific compressive stiffness of the structure decreases. This reduction in compressive stiffness is expected because, in essence, prescribing circular voids removes material that would otherwise contribute to compressive load paths. As the number of circular cavities increases, we also observe a substantial increase in radiated power. Similar to the topologies shown in Fig. 5, a greater number of circular cavities acting as heat pipes produces an approximately isothermal top surface that achieves >99% efficiency. However, in this case, the near-isothermal surface condition is easier to achieve because of the regular spacing and consistent geometry of the fixed cavity regions.

Next, we extrude the topologies with fixed circular cavities along the radiator length, and we analyze the bending stiffness and the dynamic response. Similar to the trend observed in Fig. 3, the specific bending stiffness of radiators with circular voids inversely correlates with thickness and volume fraction (Fig. 6c). As the number of circular voids increases, the specific bending stiffness increases slightly, suggesting an interplay between mass distribution and bending stiffness in radiators with circular cavities. This effect arises because the circular cavities act as stiffening features that preserve load-bearing pathways in bending, countering the stiffness reduction seen in compression. Figure 7 shows the general trends in the fundamental frequency for

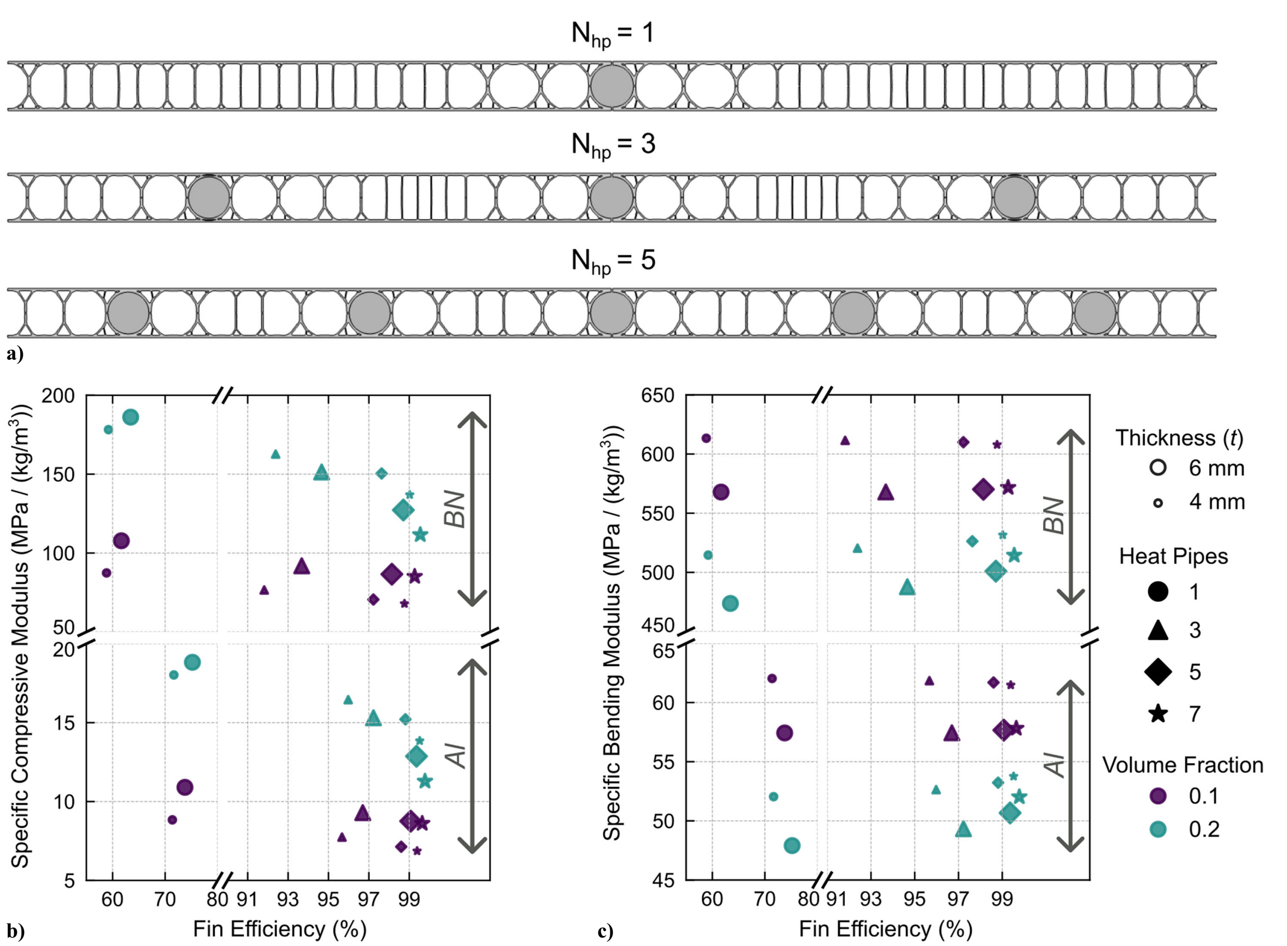

Fig. 6 a) Thermomechanical analysis of optimized radiators with fixed heat-pipe cavities. b) Specific compressive modulus versus fin efficiency. c) Specific bending modulus versus fin efficiency.

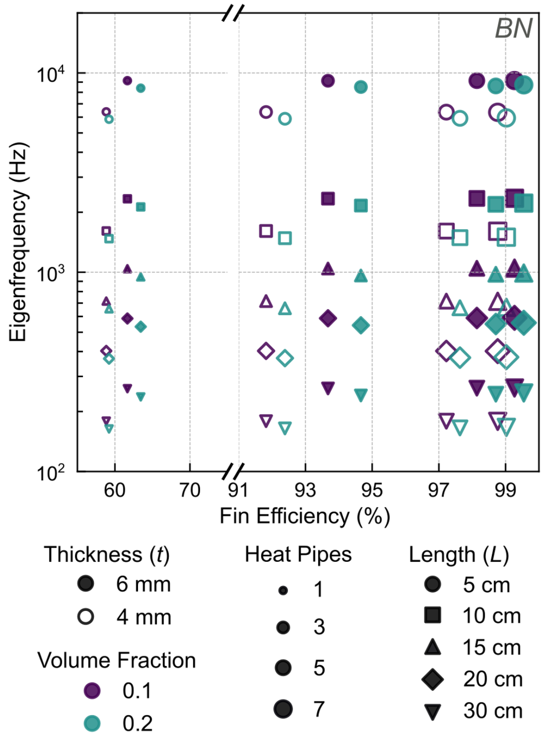

Fig. 7 Fundamental eigenfrequency versus fin efficiency.

radiators with varying lengths, thicknesses, volume fractions, and numbers of circular cavities. As before, the fundamental frequency correlates positively with radiator thickness (i.e., thicker radiators have a higher fundamental-mode resonant frequency) and negatively with volume fraction and radiator length. Interestingly, the fundamental frequency does not appear to be very sensitive to the number of circular cavities, suggesting that the dynamic response is primarily governed by global geometry and effective properties rather than localized cavity arrangement. These results collectively indicate that by prescribing protected circular cavity regions during optimization, it is possible to achieve superior thermal uniformity without compromising dynamic stability.

V. Conclusions

This study presents a broad thermomechanical design-space analysis that leverages topology optimization to explore multifunctional lightweight radiators for addressing the competing requirements of stiffness, mass, and thermal conductivity in small-satellite platforms. Our approach combines coupled structural and thermal optimization to generate hierarchical microarchitectures that naturally form continuous cavities suitable for high-conductivity channels. The parametric investigation revealed Pareto tradeoffs among mass, stiffness, and thermal performance while capturing dynamic considerations associated with the vibrational modes of the radiator. Future extensions of this analysis could incorporate full three-dimensional topology optimization to account for variations in heat-flow paths, complex stress distributions and heat inputs, and spatially varying heat-pipe or channel paths. While this study focused on two relevant material examples (i.e., a high-conductivity and a high-modulus material) to highlight the dominant trends, it would be relevant to expand this analysis to include advanced metal alloys and high-performance composites (for example, those integrating high-conductivity and high-stiffness boron nitride nanotubes [33–35]). In addition, a fully coupled thermal-fluid analysis of embedded heat channels/pipes, incorporating the effects of working-fluid phase change, would more accurately capture coupled thermofluidic behavior and its influence on system performance [36,37].

From a manufacturing perspective, the proposed architectures could be compatible with current additive manufacturing processes [38,39], with feature sizes governed by typical powder-bed fusion resolution limits. Future studies can incorporate manufacturability constraints once they are defined for a specific material system and fabrication process. For example, future implementations could impose minimum channel diameter, access pathways for depowdering, and geometric constraints on enclosed volumes. In addition, because the radiator geometries considered here are symmetric and extruded, one possible fabrication route would be to manufacture the structure in two open halves, remove residual powder from the exposed channels, and then join the halves by brazing or welding. Other approaches, such as wire electrical discharge machining (wire EDM), may also be suitable depending on the final geometry. Similarly, it would be relevant to use this framework for a matched comparison between topology-optimized cores and conventional flight-ready honeycomb radiator panels under consistent mass, thickness, thermal loading, and dynamic response constraints. Such a comparison could also incorporate details such as joining or bonding methods and system-level heat transport modeling. Future work should also consider integration with multisegment deployable radiator architectures. For example, hinge-less or self-deploying concepts based on shape-memory alloys may provide compact deployment mechanisms, while flexible or coiled heat-transport elements could maintain thermal continuity between deployed segments and the spacecraft bus [10,40]. The thermal analysis presented here does not take into account the effects of changing radiative environments on the performance of radiator panels. However, future work should explore how incorporating spectrally selective emissivity materials and coatings may aid in mitigating variable radiative thermal loads in orbit [41]. Finally, system-level integration studies that link radiator performance to spacecraft power, thermal, and structural subsystems would be critical for evaluating these multifunctional designs for flight-ready thermal control solutions [42,43].

Acknowledgments

The authors thank R. Sweat and M. Bessa for the helpful discussions. This material is based upon research supported by DARPA under Award Number D24AP00310-00. The authors acknowledge the Minnesota Supercomputing Institute (MSI) at the University of Minnesota for providing resources that contributed to the research results reported in this paper. S.K. acknowledges support through the NASA Space Technology Graduate Research Opportunities (NSTGRO) fellowship 80NSSC24K1372.

References

[1] Gilmore, D., *Spacecraft Thermal Control Handbook: Volume I: Fundamental Technologies*, Aerospace Press, Segundo, CA, 2002.

[2] Selva, D., and Krejci, D., "A Survey and Assessment of the Capabilities of Cubesats for Earth Observation," *Acta Astronautica*, Vol. 74, May-June 2012, pp. 50–68.
https://doi.org/10.1016/j.actaastro.2011.12.014

[3] Weston, S., Miller, C., Ingersoll, J., Yost, B., Agasid, E., Burton, R., Carlino, R., Defouw, G., Perez, A. D., Karacalioglu, A. G., et al., "State of the Art: Small Spacecraft Technology," NASA TR ARC-E-DAA-TN58827, 2018.

[4] Hengeveld, D., Moulton, J., Wilson, M., Taft, B., and Kwas, A., "Thermal Design Considerations for Future High-Power Small Satellites," *48th International Conference on Environmental Systems*, Texas Tech Univ. Press, Lubbock, TX, 2018.

[5] Yendler, B., Meginnis, A., and Reif, A., "Thermal Management High Power Cubesats," *34th Annual AIAA/Utah State University Small Satellite Conference*, AIAA, Reston, VA, 2020.

[6] Hager, P., and Janzer, K., "Influence of Orbit and Thermal Design Parameters on the Temperature Behaviour of CubeSats-Implications for Thermal Analysis and Thermal Hardware Demands," *2020 International Conference on Environmental Systems*, Texas Tech Univ. Press, Lubbock, TX, 2020.

[7] Nagano, H., Nagasaka, Y., and Ohnishi, A., "Simple Deployable Radiator with Autonomous Thermal Control Function," *Journal of Thermophysics and Heat Transfer*, Vol. 20, No. 4, 2006, pp. 856–864.
https://doi.org/10.2514/1.17988

[8] Meseguer, J., Pérez-Grande, I., and Sanz-Andrés, A., *Spacecraft Thermal Control*, Woodhead Publ., Cambridge, England, U.K., 2012.
[9] Cannon, J. R., Havey, K. N., Housley, N. S., Mulford, R. B., and Iverson, B. D., "Internally Stowed, Radially Deployed Radiator Panels for Passive CubeSat Thermal Control," *Applied Thermal Engineering*, Vol. 270, July 2025, Paper 126281.
https://doi.org/10.1016/j.applthermaleng.2025.126281
[10] Miesner, S., Shibata, G., Bautista, N., Wolk, K., Furst, B., Daimaru, T., Sunada, E., Roberts, S., Bellardo, J., and Kuo, J., "Thermal Orbital Spacecraft Analysis of an Additively Manufactured Deployable Radiator Oscillating Heat Pipes (AMDROHP) CubeSat," *Proceedings of the ASME 2023 International Mechanical Engineering Congress and Exposition*, Vol. 10, American Soc. of Mechanical Engineers, New York, 2023, p. V010T11A014.
https://doi.org/10.1115/imece2023-114220
[11] Vaughn, W., Shinn, E., Rawal, S., and Wright, J., "Carbon-Carbon Composite Radiator Development for the EO-1 Spacecraft," NASA TR 20040095915, Jan. 2004.
[12] Curran, D. G. T., and Lam, T. T., "Weight Optimization for Honeycomb Radiators with Embedded Heat Pipes," *Journal of Spacecraft and Rockets*, Vol. 33, No. 6, 1996, pp. 822–828.
https://doi.org/10.2514/3.26844
[13] Belfi, F., Iorizzo, F., Galbiati, C., and Lepore, F., "Space Structures with Embedded Flat Plate Pulsating Heat Pipe Built by Additive Manufacturing Technology: Development, Test and Performance Analysis," *Journal of Heat Transfer*, Vol. 141, No. 9, 2019, Paper 095001.
https://doi.org/10.1115/1.4042082
[14] Iwata, N., Saitoh, M., Yanagase, K., Iso, Y., Inoue, Y., Ogawa, H., and Miyazaki, Y., "Thermal and Structural Performance of a Small Satellite with Networked Oscillating Heat Pipes," *Journal of Spacecraft and Rockets*, Vol. 59, No. 3, 2022, pp. 1016–1028.
https://doi.org/10.2514/1.A35242
[15] Queheillalt, D. T., Carbajal, G., Peterson, G. P., and Wadley, H. N. G., "A Multifunctional Heat Pipe Sandwich Panel Structure," *International Journal of Heat and Mass Transfer*, Vol. 51, Nos. 1–2, 2008, pp. 312–326.
https://doi.org/10.1016/j.ijheatmasstransfer.2007.03.051
[16] Collicott, H., Coleman, J., and Gottschlich, J., "Spacecraft Radiator Design Using Metal Matrix Composites," *5th Joint Thermophysics and Heat Transfer Conference*, AIAA Paper 1990-1707, 1990.
https://doi.org/10.2514/6.1990-1707
[17] Noda, K., Ueno, A., and Nagano, H., "Fabrication and Testing of CFRP Embedded Oscillating Heat Pipe for Microsatellite," *49th International Conference on Environmental Systems*, Texas Tech Univ. Press, Lubbock, TX, 2019.
[18] Iwata, N., Nakanoya, S., Nakamura, N., Takeda, N., and Tsutsui, F., "Thermal Performance Evaluation of Space Radiator for Single-Phase Mechanically Pumped Fluid Loop," *Journal of Spacecraft and Rockets*, Vol. 59, No. 1, 2022, pp. 225–235.
https://doi.org/10.2514/1.A35030
[19] Smay, J., Hughes, J., Spangler, R., Tarau, C., and Alvarez-Hernandez, A., "Volatiles Investigating Polar Exploration Rover (VIPER) Thermal Management System (TMS) Design, Development, and Testing," *53rd International Conference on Environmental Systems*, Texas Tech Univ. Press, Lubbock, TX, 2024.
https://doi.org/10.32865/2346/98784
[20] Roper, C. S., "Multiobjective Optimization for Design of Multifunctional Sandwich Panel Heat Pipes with Micro-Architected Truss Cores," *International Journal of Heat and Fluid Flow*, Vol. 32, No. 1, 2011, pp. 239–248.
https://doi.org/10.1016/j.ijheatfluidflow.2010.07.002
[21] Gyányi, S., Szabolcsi, R., Varga, P. J., Horváth, G., Horváth, P., and Wührl, T., "Micro-Vibrations Analysis in LEO CubeSats Using MEMS Accelerometers," *Sensors (Basel, Switzerland)*, Vol. 25, No. 18, 2025, p. 5917.
https://doi.org/10.3390/s25185917
[22] Dennehy, C., and Alvarez-Salazar, O. S., "Spacecraft Micro-Vibration: A Survey of Problems, Experiences, Potential Solutions, and Some Lessons Learned," NASA TR 20180006315, 2018.
[23] Dennehy, C. J., Wolf, A. A., and Swanson, D. K., "Spacecraft Line-of-Sight Jitter Management and Mitigation Lessons Learned and Engineering Best Practices," NASA TR 20210017871, 2021.
[24] Shields, J., Pong, C., Lo, K., Jones, L., Mohan, S., Marom, C., and Andrade, L., "Characterization of CubeSat Reaction Wheel Assemblies," *Journal of Small Satellites*, Vol. 6, No. 1, 2017, pp. 565–580.
[25] Bendsøe, M. P., and Sigmund, O., "Material Interpolation Schemes in Topology Optimization," *Archive of Applied Mechanics*, Vol. 69, Nos. 9–10, 1999, pp. 635–654.
https://doi.org/10.1007/s004190050248
[26] Sigmund, O., "Topology Optimization: A Tool for the Tailoring of Structures and Materials," *Philosophical Transactions. Series A, Mathematical, Physical, and Engineering Sciences*, Vol. 358, No. 1765, 2000, pp. 211–227.
https://doi.org/10.1098/rsta.2000.0528
[27] Haertel, J. H. K., Engelbrecht, K., Lazarov, B. S., and Sigmund, O., "Topology Optimization of Thermal Heat Sinks," *COMSOL Conference 2015*, Technical Univ. of Denmark, Lyngby, Denmark, 2015.
[28] COMSOL, "*COMSOL Multiphysics v. 6.1*," COMSOL AB, Stockholm, Sweden, 2022.
[29] McMaster-Carr, "Electrically-Insulating Boron Nitride Ceramic Sheets and Bars: Part #84995K12," 2025, https://www.mcmaster.com/products/boron-nitride-sheets/ [retrieved 30 Dec. 2025].
[30] James, R. S., "Aluminum-Lithium Alloys," *Properties and Selection: Nonferrous Alloys and Special-Purpose Materials*, ASM International, Materials Park, OH, 1990, pp. 178–199.
https://doi.org/10.31399/asm.hb.v02.a0001063
[31] Bendsøe, M. P., and Sigmund, O., "Topology Optimization by Distribution of Isotropic Material," *Topology Optimization: Theory, Methods and Applications*, Springer, Heidelberg, 2004, pp. 1–69.
[32] Yang, X., Yan, Y. Y., and Mullen, D., "Recent Developments of Lightweight, High Performance Heat Pipes," *Applied Thermal Engineering*, Vols. 33–34, Feb. 2012, pp. 1–14.
https://doi.org/10.1016/j.applthermaleng.2011.09.006
[33] Kim, J. H., Pham, T. V., Hwang, J. H., Kim, C. S., and Kim, M. J., "Boron Nitride Nanotubes: Synthesis and Applications," *Nano Convergence*, Vol. 5, No. 17, 2018.
https://doi.org/10.1186/s40580-018-0149-y
[34] Tank, M., and Sweat, R., "Boron Nitride Nanotubes (BNNTs) and BNNT Composites: A Review," *Materials Performance and Characterization*, Vol. 11, No. 1, 2022, pp. 278–312.
https://doi.org/10.1520/MPC20220042
[35] Tank, M., Leon, A. D., Huang, W., Patadia, M., Degraff, J., and Sweat, R., "Manufacturing of Stereolithographic 3D Printed Boron Nitride Nanotube-Reinforced Ceramic Composites with Improved Thermal and Mechanical Performance," *Functional Composites and Structures*, Vol. 5, No. 1, 2023, Paper 015001.
https://doi.org/10.1088/2631-6331/acb12a
[36] Patel, V. K., "An Efficient Optimization and Comparative Analysis of Ammonia and Methanol Heat Pipe for Satellite Application," *Energy Conversion and Management*, Vol. 165, June 2018, pp. 382–395.
https://doi.org/10.1016/j.enconman.2018.03.076
[37] Turgut, O. E., and Çoban, M. T., "Thermal Design of Spiral Heat Exchangers and Heat Pipes Through Global Best Algorithm," *Warme- und Stoffubertragung [Heat and Mass Transfer]*, Vol. 53, No. 3, 2017, pp. 899–916.
https://doi.org/10.1007/s00231-016-1861-y
[38] Sacco, E., and Moon, S. K., "Additive Manufacturing for Space: Status and Promises," *International Journal of Advanced Manufacturing Technology*, Vol. 105, No. 10, 2019, pp. 4123–4146.
https://doi.org/10.1007/s00170-019-03786-z
[39] Kabir, M., Preller, E., Mohammed, R., Tarau, C., Yang, B., Alvarez-Hernandez, A., and Xu, J., "Investigation of an Additively Manufactured Two-Phase Heat Exchanger with Built-in Thermal Storage," *2023 22nd IEEE Intersociety Conference on Thermal and Thermomechanical Phenomena in Electronic Systems (ITherm)*, Inst. of Electrical and Electronics Engineers, New York, 2023.
https://doi.org/10.1109/itherm55368.2023.10177646
[40] Santana, M., Kuo, J., Bellardo, J., Roberts, S., Sunada, E., and Daimaru, T., "Evaluation of Nitinol Shape Memory Alloy Actuators for a Deployable CubeSat Radiator," *Proceedings of the ASME 2025 International Mechanical Engineering Congress and Exhibition*, Vol. 3, American Soc. of Mechanical Engineers, New York, 2025, p. V003T06A009.
https://doi.org/10.1115/imece2025-168023.
[41] Kauder, L., "Spacecraft Thermal Control Coatings References," NASA Goddard Space Flight Center, NASA TP 2005-212792, 2005.
[42] Kontaxoglou, A., Tsutsumi, S., Khan, S., and Nakasuka, S., "Multifidelity Framework for Small Satellite Thermal Analysis," *Journal of Spacecraft and Rockets*, Vol. 61, No. 1, 2023, pp. 61–71.
https://doi.org/10.2514/1.A35666
[43] Chipps, A., Forgette, D., and Cahoy, K., "SATMO: A Multi-Planet Thermal Analysis Tool for CubeSat Missions," *AIAA SciTech 2026 Forum. Session: Thermal Control and Heat Transfer I*, AIAA Paper 2026-2269, 2026.
https://doi.org/10.2514/6.2026-2269

T. J. Prater
Associate Editor